Peer-reviewed version available at *Actuators* **2020**, *9*, 28; doi:10.3390/act9020028

Article

Multi-Physical Design and Resonant Controller Based Trajectory Tracking of the Electromagnetically Driven Fast Tool Servo

Imran Hussain [1], Wei Xia [1], Dongpo Zhao [1], Peng Huang [2,*] and Zhiwei Zhu [1]

[1] School of Mechanical Engineering, Nanjing University of Science and Technology (NJUST), Nanjing 210094, China; imranbagoro_128@yahoo.com

[2] College of Mechatronics and Control Engineering, Shenzhen University (SZU), Shenzhen, G.D. 518060, China; huangp@szu.edu.cn.

* Correspondence: huangp@szu.edu.cn (Peng Huang)

Abstract: In this paper, a voice coil motor (VCM) actuated fast tool servo (FTS) system is developed for diamond turning. To guide motions of the VCM actuator, a crossed double parallelogram flexure mechanism is selected featuring totally symmetric structure with high lateral stiffness. To facilitate the determination of the multi-physical parameters, analytical models of both electromagnetic and mechanical systems are developed. The designed FTS with balanced stroke and natural frequency is then verified through the finite element analysis. Finally, the prototype of the VCM actuated FTS is fabricated and experimentally demonstrated to have a stroke of ±59.02 μm and a first natural frequency of 253 Hz. By constructing a closed-loop control using PID controller with the internal-model based resonant controller, the error for tracking a harmonic trajectory with ±10 μm amplitude and 120 Hz frequency is obtained to be ±0.2 μm, demonstrating the capability of the FTS for high accuracy trajectory tracking.

Keywords: Fast Tool Servo; Voice coil motor; Flexure mechanism; Resonant Controller

1. Introduction

Fast Tool Servo (FTS) is a promoting servo axis that is widely engaged in combination with diamond turning that oscillates the diamond tool several times in each rotation of the workpiece clamped on the spindle [1]. With the FTS system, it mainly consists of three subsystems, including the actuator to drive the cutting tool, the guiding mechanism to guide the motion of the actuator, and the feedback control system to guarantee the motion accuracy.

Within the last three decades, much effort has been devoted to improving performance of FTS system. In general, the actuator performs an important task with which the performance of FTS system is fundamentally determined. Nowadays, the piezoelectric actuators (PEA) [2, 3] and the Lorentz electromagnetic force-based voice coil motor (VCM) [4, 5] are the two most popular driving sources for FTS. Although the PEA has many unique advantages, it is strongly restricted by its small motion stroke, and accordingly, the deliberately designed flexure mechanisms are required to amplify the motions of the PEA for large stroke application. To satisfy the turning of freeform surfaces with large sagitta values, the VCM would be a better choice. For example, the VCM driven long stroke FTS developed in [4] and [5], for which a commercial VCM and a crossed leaf-type flexure hinge were adopted. With respect to the major of commercially available VCMs, the center part is fulfilled by soft magnetic material to construct the magnetic circuit [4, 5]. Although it is convenient for the VCM design, there is a challenge for placing the sensors to capture the motion of the tool.

With the VCM actuated FTS, the air bearing and flexure mechanism are two basic guidance mechanism to support and guide the motion of the tool. Usually, the air bearing can achieve quite long stroke motion without mechanical contact. However, the air-bearing cost is very high due to the

tight manufacturing and assembly tolerance of its key components [6]. The flexure mechanism with low cost is promising to serve as the bearing for guiding motions in the micro-meter scale up to the millimeter scale [4, 5]. Therefore, it is more efficient to work for the short and medium stroke FTS. Currently, the design of the flexure mechanism mainly focused on the stiffness along the desired motion direction, and the lateral stiffness was mainly ignored which is especially important for FTS turning considering the cutting force in the free space.

Another issue related to the VCM actuated FTS would be the tracking accuracy of the trajectory. Since force density of the VCM is essentially low, the VCM actuated FTS usually has very limited bandwidth which will normally lead to a poor trajectory tracking accuracy for high-frequency trajectory tracking. Considering the (quasi-)periodic nature of the trajectory for FTS diamond turning of freeform surfaces, the repetitive control (RC) was developed to ultra-finely track the components with specified frequencies [7]. However, with the RC, a low-pass filter is essentially required to stabilize the control system which will deteriorate the tracking accuracy, especially when the tracking frequency approaches the cut-off frequency of the filter. Furthermore, design of the RC corresponding to the trajectory with multiple harmonic components which do not share the same fundamental frequency would be more complicated. The resonant controller (or called the adaptive feedforward cancellation, AFC [8, 9]) using a set of parallel resonators to ultra-finely track the trajectory components with the resonant frequency is very promising for accurately track the (quasi-) periodic trajectory in a simple and effective way. It was demonstrated to be effective for FTS turning driven by the normal-stressed electromagnetic force [9].

With these aforementioned discussions on the three main aspects of the FTS, the multi-physical parameters of both the electromagnetic and mechanical part of a VCM actuated FTS is deliberately designed. The electromagnetic circuit is designed to leave a space for placing the capacitive sensor to sufficiently capture the unidirectional motion of the tool, and a crossed flexure mechanism using four sets of identical parallelogram mechanisms is designed to improve the lateral stiffness. Finally, the resonant controller is applied to achieve a high accuracy for high-frequency trajectory tracking.

2. Architecture of the VCM Actuated FTS System

The three-dimensional design of the VCM actuated FTS system is illustrated in Fig. 1. The armature of a cuboid-shaped VCM was designed to be fixed with the single-axis flexure mechanism. With the flexure mechanism, a crossed double parallelogram mechanism was designed to simultaneously improve the axial motion accuracy and the lateral stiffness to effectively bear the spatial cutting force. To guarantee a good capture of the tool motion, a capacitive displacement sensor is arranged through the center of the VCM to target at the center of the tool holder, which agrees with the center axis of the motion.

The working principle of the VCM actuated FTS is further shown in Fig. 1(b). A Lorentz-force generated by the interaction between the magnetic field and the coil carrying the current. The force drives the armature which is fixed with the flexure mechanism. In principle, the generated force (Fa) is proportional to the input current, flux density, and equivalent length of the coil inside the magnetic field, which is [10].

$$F_a = \int idl \times B_{av} \equiv ilB_{av} = B_{av} i(N_T l) \tag{1}$$

where $i, l, and\ B_{av}$ are the applied current, the length of coil within the magnetic field, and average magnetic flux density in the air gap. N_T represents numbers of turns in case of multiple numbers of turns in the coil.

Preprints (www.preprints.org) | NOT PEER-REVIEWED | Posted: 11 March 2020 doi:10.20944/preprints202003.0179.v1

Peer-reviewed version available at Actuators 2020, 9, 28; doi:10.3390/act9020028

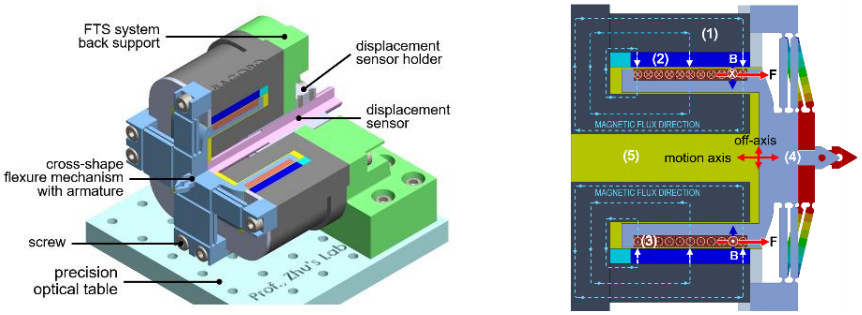

(a) (b)

Figure 1. Mechanical structure of the VCM actuated FTS system, (a) the zonal-sectional view, and (b) the cross-section view of the assembled structure, where (1) stator, (2) permanent magnet, (3) coil, (4) mover, (5) air-gap

2.1 Design of the voice coil motor

In the cuboid-shaped structure of VCM, the major parts consist of a stator (core and yoke), permanent magnet (PM), coil, and mover (joint design of armature of VCM and flexure hinge) as shown in Fig. 1. The PM is a source to generate magnetic flux, these magnetic fluxes cross the small air-gap and enter into the coil and armature, and then connect with stator. Finally, a complete closed-loop path is developed for magnetic flux inside the VCM body as illustrated in Fig. 1(b).

Focusing the coil configuration, Assume $l_c = dia \times N_t$ and $h_c = dia \times N_l$ are the efficient length and height for multiple turns and layers in the coil as shown in Fig. 3. The total number of turns (N_T) in the coil can be expressed by $N_T = N_t \times N_l$. The total length for a single turn in coil is $4w$ that is within the magnetic field where w is the width of PM. The equivalent length of coil can be expressed as $l = 4w \times N_T$. The parameters for the armature where coil is made is given in Table 1.

Table 1. Selected parameters for coil configuration, (copper wire (AWG23, 0.57mm diameter)).

Symbol	Description	Turns/Layers	Value
l_c	Length for multiple turns	64	37mm
h_c	height for multiple turns	8	4.5mm
N_T	Total number of turns	64 x 8	512

In material selection, NdFeB (N52) was selected for the PM whose magnetic remanence is 1.47T. Soft iron (AISI 1010) was chosen for the stator, whose relative permeability is nonlinear. Copper wire (AWG23) with a current rating 3 ampere is selected for the winding. Aluminum is selected for the mover. The PM holder is designed to support and hold PMs inside the yoke. High reluctant material is selected for PM holder so that it can stop the leakage flux from the sides of PM. A relatively high air-gap is kept at the back of armature in the moving axis to provide free reciprocating motion. The selected geometric parameters of VCM is given in Table 2.

Table 2. Selected geometric parameters of voice coil motor (unit: mm).

Parts	Geometric parameters	Symbols	Value
Stator	thickness (outer side of yoke)	t_y	10
	thickness (central iron core)	t_{cr}	12
PM	length	$l_c + 3$	40
	thickness (magnetization direction)	t_{PM}	5
	width	w	50
Armature	thickness	-	4.5
Air-gap	thickness	t_{ag}	0.5

Preprints (www.preprints.org) | NOT PEER-REVIEWED | Posted: 11 March 2020 doi:10.20944/preprints202003.0179.v1

Peer-reviewed version available at Actuators 2020, 9, 28; doi:10.3390/act9020028

2.2. Design of the flexure mechanism

As shown in Fig. 1, a flexure mechanism using two crossed identical double parallelogram mechanisms is designed to connect with the armature. As illustrated in Fig. 2, each parallelogram mechanism consists of two parallel linkages, and each linkage is serially connected by two right-circular flexure hinges (RCFH) and one rectangular leaf-spring flexure hinge (LSFH) with thickness b. The RCFH provides relative rotation between two adjutant rigid members through elastic bending. The crossed double parallelogram mechanisms will not only support the desired unidirectional motion, but also constrain the undesired parasitic motions with enhanced lateral stiffness.

In general, the structural dimensions as marked in Fig. 2 will greatly influence the working performance of the mechanism. Through manually tuning the parameters affiliated by the system models as established in section 3, the selected parameters are summarized in the Table 3 to meet the desired motion stroke and natural frequency.

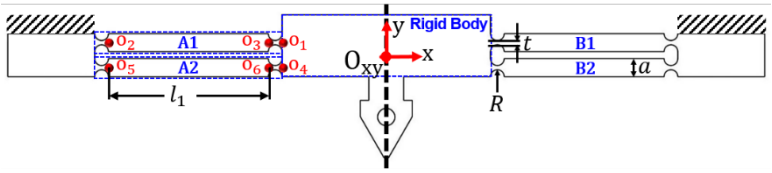

Figure 2. Cross-section view of the double parallelogram flexure mechanism.

Table 3. Design parameters of flexure mechanism (unit: mm).

R	t	l_1	a	b
1	0.6	28	2.6	30

3. Modeling and verification of the VCM actuated FTS system

3.1. Magnetic Equivalent Circuit modeling

The magnetic equivalent circuit (MEC) modeling can be used to find magnetic flux densities at any point in the magnetic circuit. The mathematical expressions for magnetic flux densities can be obtained by approximations with magnetic circuit elements [11, 12]. An axis-symmetry cross-section view of the magnetic circuit of the designed VCM is illustrated in Fig. 3, where all structural parameters are represented with lumped circuit elements.

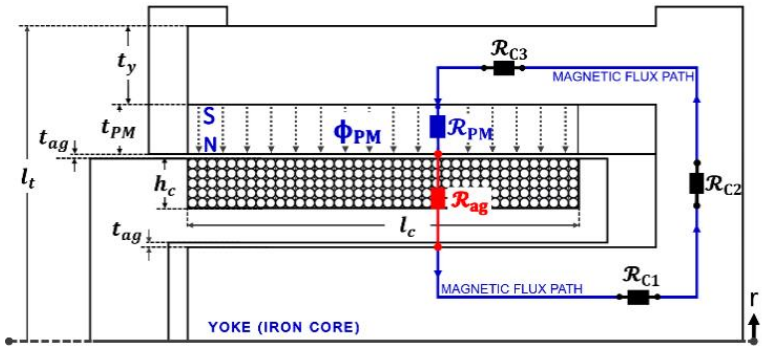

Figure 3. Lumped-circuit element based magnetic circuit model of the VCM, where t_{PM}, t_{ag}, and t_y are the thickness of PM, air-gap, and yoke, respectively. l_t is the length from the outer to the axis of the VCM. $\mathcal{R}_{c1}$, $\mathcal{R}_{c2}$, and $\mathcal{R}_{c3}$ are the equivalent reluctance of the stator material.

With the equivalent circuit shown in Fig. 2, the magneto-motive force (F_m) generated from PM can be expressed by [11, 12].

Peer-reviewed version available at Actuators 2020, 9, 28; doi:10.3390/act9020028

$$F_m = \frac{B_r t_{PM}}{\mu_{PM}} \tag{2}$$

where $B_r = 1.47\ T$ is the remanence of the PM, and μ_{PM} is the relative permeability of the PM material. Ignoring the reluctance of the stator and the leakage flux, the reluctance of the PM and air-gap can be approximately expressed by [11, 12]

$$\mathcal{R}_{PM} = \frac{t_{PM}}{\mu_{PM} A_{PM}} \tag{3}$$

$$\mathcal{R}_{ag} = \frac{t_{ag}}{\mu_{ag} A_{ag}} \tag{4}$$

where, A_{PM}, and A_{ag} are the cross-section area of PM and air-gap, and the relative permeability inside the air-gap is μ_{ag}.

The general magnetic flux expression can be expressed using Ohm's law for the equivalent magnetic circuit, and the magnetic flux density (B_{ag}) inside the air-gap can be obtained as

$$B_{ag} = \frac{\Phi_{av}}{A_{ag}} = \frac{F_m}{A_{ag}(\mathcal{R}_{PM} + \mathcal{R}_{ag})} = \frac{B_r t_{PM}}{\mu_{PM} A_{ag}(\mathcal{R}_{PM} + \mathcal{R}_{ag})} \tag{5}$$

3.2. Modeling of flexure mechanism

To obtain the stiffness of the developed flexure mechanism, the matrix-based compliance modeling (MCM) method is adopted [3, 13]. Following the MCM method, the compliance C_{A1} and C_{A2} of the flexible linkages A1 and A2 can be expressed in the global coordinate system as

$$\mathrm{C}_{A1}^{o} = T_{O_1} C_{O_1}^{R} \left(T_{O_1}\right)^{T} + T_{O_2} C_{O_2}^{R} \left(T_{O_2}\right)^{T} + T_3 C_{O_3}^{L} \left(T_{O_3}\right)^{T} \tag{6}$$

$$\mathrm{C}_{A2}^{o} = T_{O_4} C_{O_4}^{R} \left(T_{O_4}\right)^{T} + T_{O_5} C_{O_5}^{R} \left(T_{O_5}\right)^{T} + T_{O_6} C_{O_6}^{L} \left(T_{O_6}\right)^{T} \tag{7}$$

where $C_{O_{\mathrm{i}}}^{R}$ and $C_{O_{\mathrm{i}}}^{L}$ represent the basic matrix of the RCFH [14] and LSFH [15] locally expressed in the system Oi, and $T_{O_{\mathrm{i}}}$ means the coordinate transfer matrix from system Oi to the global system [13].

Considering the parallel configuration of the two parallel linages (A1 and A2), the total compliance of A1 and A2 at O_{xy} can be expressed by

$$C_L^o = \left((C_{A1}^o)^{-1} + {C_{A2}^o}^{-1}\right)^{-1} \tag{8}$$

Similarly, the total compliance of the double parallelogram mechanism can be obtained as

$$C_{dp}^o = \left({C_L^o}^{-1} + (TY(\pi)\, C_L^o\, (TY(\pi))^T)^{-1}\right)^{-1} \tag{9}$$

where $TY(\pi)$ is the transformation matrix around the y-axis with an angle of π. Taking advantage of symmetric structure of flexure hinge, the resultant stiffness of the flexure mechanism can be expressed by

$$K^o = {C_{dp}^o}^{-1} + \left(TZ\left(\frac{\pi}{2}\right)\, C_{dp}^o \left(TZ\left(\frac{\pi}{2}\right)\right)^T\right)^{-1} \tag{10}$$

where $TZ(\pi/2)$ is the transformation matrix around the y-axis with an angle of $\pi/2$. Considering the symmetric feature of the mechanism, its input stiffness can be obtained as $k_{in} = K^o\,(2,2)$. Considering the maximum current carried by the coil, the maximum stroke can be derived as

$$s = \frac{B_{av} I_{max} (N_T l)}{k_{in}} \tag{11}$$

where I_{max} is the maximum allowable current of the coil, which is selected as 1.6 A in this study.

Preprints (www.preprints.org) | NOT PEER-REVIEWED | Posted: 11 March 2020 doi:10.20944/preprints202003.0179.v1

Peer-reviewed version available at Actuators 2020, 9, 28; doi:10.3390/act9020028

The flexure mechanism regards as an equivalent damped mass-spring system from dynamic point of view [16]. Lagrangian equation is used to derive the dynamic model [16]. Taking advantage of the symmetric structure of the flexure mechanism, the kinetic energy can be obtained as

$$T = \frac{I_y}{2}\left(\frac{\dot{x}}{l_1}\right)^2 n_l + \frac{m_1}{2}\dot{x}^2 \tag{12}$$

where, x is the generalized coordinate, $n_l = 8$, I_y is the moment of inertia of the flexure hinge, and m_1 is the mass of the end-effector. Using Lagrangian equation, the equivalent moving mass M can be expressed by [16]

$$M = \frac{\partial T}{\partial \dot{x}} = m_1 + m_c + \frac{n_l I_y}{{l_1}^2} \tag{13}$$

Therefore, the first natural frequency of the VCM actuated FTS system can be obtained by

$$f_o = \frac{1}{2\pi}\sqrt{\frac{k_{in}}{M}} \tag{14}$$

3.3. Finite Element Analysis (FEA) validation

3.3.1. Electromagnetic verification of the VCM

To validate the respective analytical models of the VCM actuated FTS system, finite element analysis (FEA) is carried out in ANSYS workbench. To validate the MEC modeling, a magnetostatic analysis is conducted. The total magnetic flux density distribution inside the magnetic circuit of VCM is shown in Fig. 4. The average magnetic flux density inside the air-gap is observed to be about 0.383 T, and a relative modeling error of about 12.79% is obtained considering value of 0.432 T for the analytical result. The FEA and analytical results are comparatively summarized in Table 4.

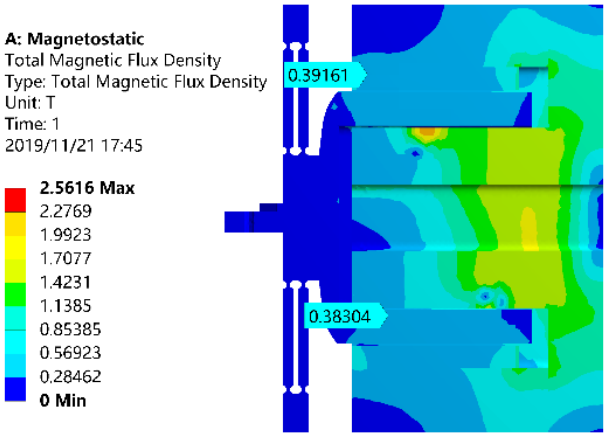

Figure 4. Distribution of the magnetic flux density obtained by FEA.

3.3.2. Mechanical verification of flexure mechanism

To validate the stiffness model, a static structural analysis is conducted. The aluminum alloy was selected for the simulation which has a modulus of elasticity is 69 GPa, passion ratio of 0.33, and mass density of 2770 kgm-3. The constrain was applied as shown in Fig. 5(a), where plane A is fixed-end and plane B is free-end. To mesh the body, a proximity and curvature-based function is selected for the finest meshing, and the meshed body is shown in Fig. 5(b).

Through applying a force of F=100 N on the free-end along the actuation direction, the total deformation of 99.428 μm is obtained as shown in Fig. 5(c) which suggests a stiffness of 1.01 N/μm.

Preprints (www.preprints.org) | NOT PEER-REVIEWED | Posted: 11 March 2020 doi:10.20944/preprints202003.0179.v1

Peer-reviewed version available at Actuators 2020, 9, 28; doi:10.3390/act9020028

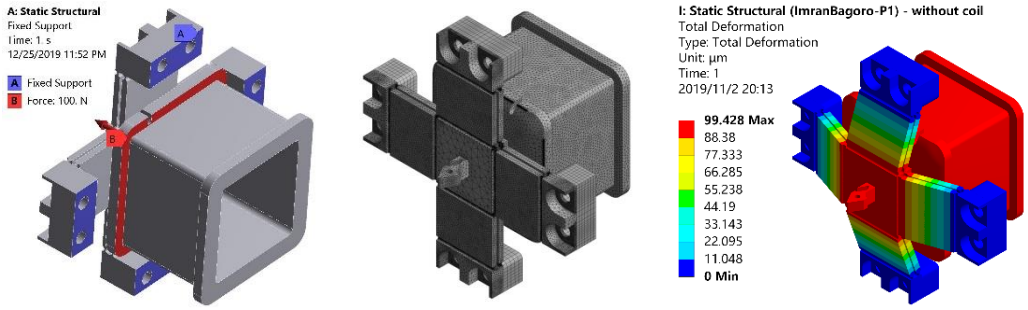

Figure 5. Static structural analysis of the flexure mechanism, (a) the constraint, (b) the meshed model, and (c) the resultant deformation with F=100 N.

Moreover, to confirm the dynamic model, the modal analysis is conducted using the same constrains, mesh, and material. From the modes shown in Fig. 6, the first natural mode agrees well with the desired motion, and the first natural frequency with and without considering the mass of coil are obtained to be 377.95 Hz and 229.91 Hz, respectively. From the comparative result summarized in Table 4, the maximum modeling error for both electromagnetic and mechanical part is less than 13%, suggesting that the developed model is reliable for the analysis and design of the VCM actuated FTS.

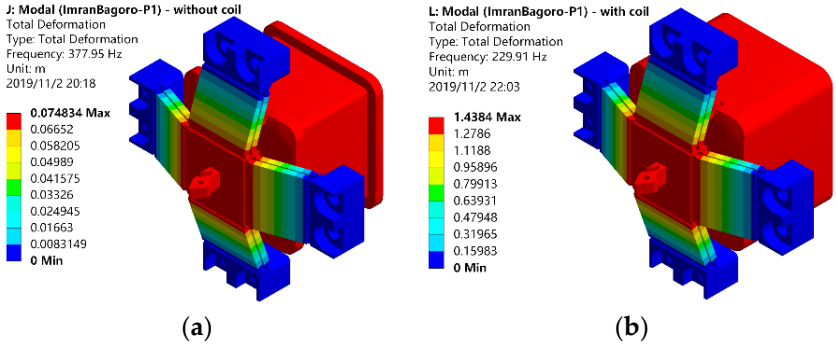

Figure 6. Modal analysis of the flexure mechanism, (a) the first mode without coil, and (b) the first mode with coil.

Table 4. The analytical and FEA results of the FTS.

	k_{in} (N/µm)	f_o (Hz)		B (T)	F_{VCM} (N)	s(µm)
		without coil	with coil			
Ana.	1.10	395.51	240.51	0.432	132.7	120.63
FEA	1.01	377.95	229.91	0.383	117.6	116.49
Error	8.91%	4.65%	4.61%	12.79%	12.78%	3.55%

4. Controller design for the Fast Tool Servo System

The control system adopts the PID controller as the control inner loop, and the outer loop adopts the adaptive feed-forward cancellation (AFC) controller to complete the tracking of the tool trajectory.

4.1. PID controller

A typical PID controller is employed as the main controller for feedback control of the system, and the parameters are tuned through the loop-shaping method as reported in [17]. During the tuning, a desired open loop transfer function $L_d(s)$ is adopted which is expressed by $L_d(s) = \omega_c/s$, where ω_c is the design expected frequency.

Peer-reviewed version available at Actuators 2020, 9, 28; doi:10.3390/act9020028

4.2. Resonant controller

In the actual cutting process, the input signal and the external interference signal can be mainly decomposed into a series of harmonic signals [8]. Therefore, the resonant controller following the repetitive control principle is used to improve the tracking accuracy, and the main control loop is illustrated in Fig. 7.

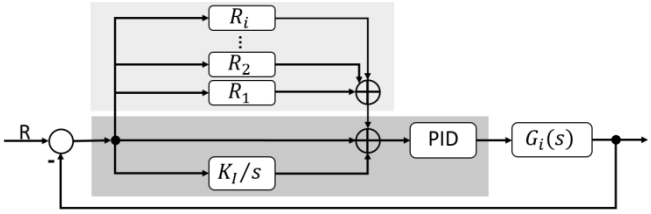

Figure 7. Control loop for the VCM actuated FTS system.

With respect to the resonant controller, the resonator can be expressed by [8]

$$R_i(s) = g_i \frac{scos\Phi_i + \omega_i sin\Phi_i}{s^2 + {\omega_i}^2} \tag{15}$$

where g_i is a proportional gain for the i-th resonator. From Eqn. (15), the phase advance angle (ϕ_i) is used to adjust the zero position of the controller [8]. The ϕ_i obtained from the Bode diagram of the system after the introduction of PID control. With respect to the control process, the frequency (ω_i) needs to be consistent with the desired frequency of the input signal.

5. Experimental Testing and Results

5.1. Experimental setup

Scheme of the testing system is shown in Fig. 8(a), and a photography of the developed prototype is shown in Fig. 8(b). For the testing, a personal computer is used to generate a digital control signal via the data acquisition (DAQ) board through the Desktop Real-time modulus in Matlab/Simulink. The servo amplifier amplifies the voltage signal with a constant gain of 0.8 A/V for driving the mover of the FTS system. A capacitive sensor measures the motion and then delivers it to the DAQ board. Both open-loop and closed-loop testing were conducted through the Desktop Real-time modulus with a sampling frequency of 20 kHz.

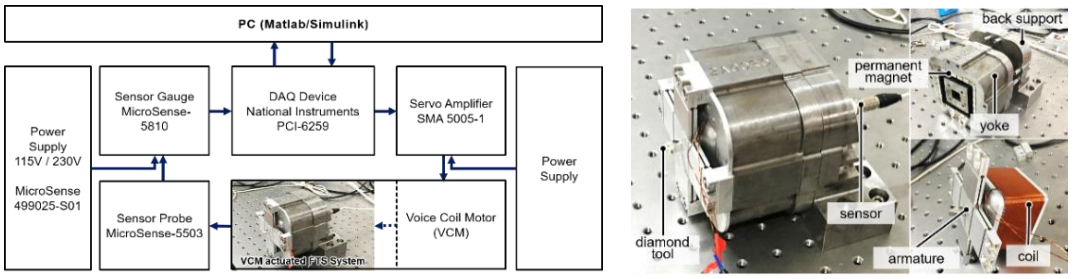

(**a**) (**b**)

Figure 8. Experimental setup, (a) schematic of the testing system, and (b) the photography of the prototype.

5.2. Experimental results

5.2.1. Static and dynamic performance testing

To study the motion range, the stroke of the FTS system subjecting to a sinusoidal command with an amplitude of 2 V was measured which led to a current of 1.6 A on the coil. The resulting stroke related to the sinusoidal command is shown in Fig. 9(a). The resulting stroke may range from

Preprints (www.preprints.org) | NOT PEER-REVIEWED | Posted: 11 March 2020 doi:10.20944/preprints202003.0179.v1

Peer-reviewed version available at Actuators 2020, 9, 28; doi:10.3390/act9020028

-62.71 μm to 53.33 μm, showing a maximum stroke around ±59.02 μm. Moreover, a sweep excitation using a harmonic command with small amplitude and linearly varying frequency from 1 Hz to 1 kHz was conducted to get the frequency response feature. From the sharp peak of frequency response in Fig. 9(b), the first natural frequency was identified to be about 253 Hz.

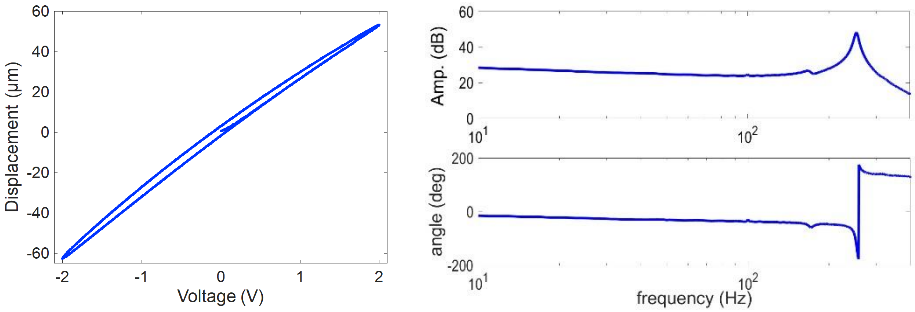

(a) (b)

Figure 9. Response of experimental testing of the FTS system, (a) the output motion related to the applied voltage, and (b) the frequency response function.

5.2.2. Control performance testing

The basic control performance test was conducted to track a harmonic signal with amplitude of 20 μm and frequency of 20 Hz, and the results are shown in Fig. 10(a). In this case, the designed controller can track the trajectory well, and the tracking error shown in Fig. 10(b) suggests a relative error of about ±0.02%. Furthermore, a tracking of the harmonic signal with frequencies of 40 Hz, 60 Hz, 80 Hz, 100 Hz and 120 Hz is performed. The tracking errors are illustrated in Figs. 10b, 10c, and 10d, and the tracking results are then summarized in Table 5 with the relative tracking errors.

From Figs. 10a, 10b, and 10c, the tracking error obviously increases with the increase of the desired frequencies. The position tracking error increased from 0.04 μm to 0.2 μm, and the relative position tracking error increased from ±0.2% to ±1%. When the frequency is higher than 120 Hz, the controller does not have a good tracking effect.

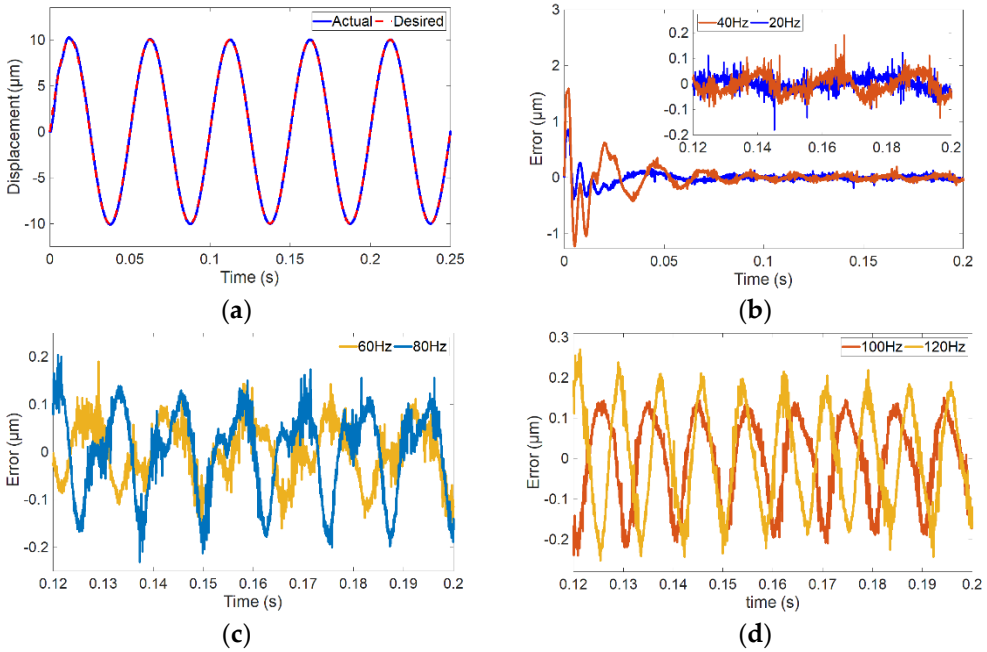

(a) (b) (c) (d)

Figure 10. The control performance, (a) tracking response for 20 Hz harmonic trajectory, (b) tracking error for 20 Hz and 40 Hz trajectory, (c) tracking error for 60 Hz and 80 Hz trajectory, and (d) tracking error for 100 Hz and 120 Hz trajectory.

Table 5. Summarized tracking error in terms of different frequencies.

Freq. (Hz)	20	40	60	80	100	120
Error (μm)	±0.040	±0.067	±0.100	±0.128	±0.144	±0.200
Percentage	±0.02%	±0.034%	±0.05%	±0.64%	±0.72%	±1.00%

6. Conclusions

A voice coil motor (VCM) actuated fast tool servo (FTS) system was developed for diamond turning. The two essential components namely the actuator and flexure mechanism are deliberately designed to balance stroke and natural frequency. To facilitate the design of structural parameters of each component, the equivalent magnetic circuit model and matrix based compliance model are established for the VCM and flexure mechanism, respectively. Finite element analysis on the magnetostatic, static structural, and model analysis is conducted to validate the designed system. The prototype of the VCM actuated FTS system is tested to have a stroke of ±59.02 μm and first natural frequency of 253 Hz. By constructing a closed-loop control using PID controller with the parallel resonant controllers, the error for tracking a set of harmonic commands with different frequencies is summarized. It suggests that although the tracking error increases with the increase of the tracking frequency, only ±1% maximum error is obtained when tracking a 120 Hz harmonic trajectory.

Author Contributions: Conceptualization, P.H. and Z.Z.; methodology, I.H. and W.X.; software, I.H. and D.Z.; formal analysis, I.H.; investigation, I.H. and W.X.; resources, X.X.; data curation, I.H., W.X., and D.Z.; writing—original draft preparation, I.H.; writing—review and editing, Z.Z.; visualization, I.H.; supervision, Z.Z.; project administration, Z.Z.; funding acquisition, P.H. and Z. Z.. All authors have read and agreed to the published version of the manuscript.", please turn to the CRediT taxonomy for the term explanation. Authorship must be limited to those who have contributed substantially to the work reported.

Funding: This research was funded by National Natural Science Foundation of China, grant number 51705254; Young Innovation Talents Program of Universities in Guangdong Province, grant number 2018KQNCX217.

Conflicts of Interest: The authors declare no conflict of interest. The funders had no role in the design of the study; in the collection, analyses, or interpretation of data; in the writing of the manuscript, or in the decision to publish the results.

References

1. Rakuff, S. and J.F. Cuttino, *Design and testing of a long-range, precision fast tool servo system for diamond turning.* Precision Engineering, 2009. **33**(1): p. 18-25.
2. Zhu, W.-L., et al., *Design and adaptive terminal sliding mode control of a fast tool servo system for diamond machining of freeform surfaces.* IEEE Transactions On Industrial Electronics, 2017. **66**(6): p. 4912-4922.
3. Zhu, Z., et al., *Development of a piezoelectrically actuated two-degree-of-freedom fast tool servo with decoupled motions for micro-/nanomachining.* Precision Engineering, 2014. **38**(4): p. 809-820.
4. Liu, Q., et al., *A Quasiphysics Intelligent Model for a Long Range Fast Tool Servo.* The Scientific World Journal, 2013. **2013**.
5. Liu, Q., et al., *Long-stroke fast tool servo and a tool setting method for freeform optics fabrication.* Optical Engineering, 2014. **53**(9): p. 092005.
6. Byl, M.F., *Design and control of a long stroke fast tool servo*. 2005, Massachusetts Institute of Technology.
7. Crudele, M. and T.R. Kurfess, *Implementation of a fast tool servo with repetitive control for diamond turning.* Mechatronics, 2003. **13**(3): p. 243-257.

8. Byl, M.F., S.J. Ludwick, and D.L. Trumper, *A loop shaping perspective for tuning controllers with adaptive feedforward cancellation.* Precision Engineering, 2005. **29**(1): p. 27-40.
9. Lu, X., *Electromagnetically-driven ultra-fast tool servos for diamond turning*. 2005, Massachusetts Institute of Technology.
10. Brauer, J.R., *Magnetic actuators and sensors*. 2006: John Wiley & Sons.
11. Okyay, A., M.B. Khamesee, and K. Erkorkmaz, *Design and optimization of a voice coil actuator for precision motion applications.* IEEE Transactions on Magnetics, 2014. **51**(6): p. 1-10.
12. Parmar, G., et al. *A moving magnet actuator for large range nanopositioning*. in *ASME 2011 Dynamic Systems and Control Conference and Bath/ASME Symposium on Fluid Power and Motion Control*. 2011. American Society of Mechanical Engineers Digital Collection.
13. Zhu, Z., et al., *A simple compliance modeling method for flexure hinges.* Science China Technological Sciences, 2015. **58**(1): p. 56-63.
14. Wu, Y. and Z. Zhou, *Design calculations for flexure hinges.* Review of scientific instruments, 2002. **73**(8): p. 3101-3106.
15. Koseki, Y., et al., *Kinematic analysis of a translational 3-dof micro-parallel mechanism using the matrix method.* Advanced Robotics, 2002. **16**(3): p. 251-264.
16. Zhu, Z., et al., *Multi-objective optimum design of fast tool servo based on improved differential evolution algorithm.* Journal of mechanical science and technology, 2011. **25**(12): p. 3141-3149.
17. Sadeghpour, M., V. De Oliveira, and A. Karimi, *A toolbox for robust PID controller tuning using convex optimization.* IFAC Proceedings Volumes, 2012. **45**(3): p. 158-163.